Optimum Aerodynamic Design of Centrifugal Compressor using a Genetic Algorithm and an Inverse Method based on Meridional Viscous Flow Analysis

Sasuga Itou, Nobuhito Oka, Masato Furukawa, Kazutoyo Yamada, Seiichi Ibaraki, Kenichiro Iwakiri, Yoshihiro Hayashi

To cite this version:

Sasuga Itou, Nobuhito Oka, Masato Furukawa, Kazutoyo Yamada, Seiichi Ibaraki, et al.. Optimum Aerodynamic Design of Centrifugal Compressor using a Genetic Algorithm and an Inverse Method based on Meridional Viscous Flow Analysis. 17th International Symposium on Transport Phenomena and Dynamics of Rotating Machinery (ISROMAC2017), Dec 2017, Maui, United States. ⟨hal-02981000⟩

HAL Id: hal-02981000

https://hal.science/hal-02981000v1

Submitted on 27 Oct 2020

Optimum Aerodynamic Design of Centrifugal Compressor using a Genetic Algorithm and an Inverse Method based on Meridional Viscous Flow Analysis

Sasuga Itou [1]*, Nobuhito Oka [2], Masato Furukawa [1], Kazutoyo Yamada [1],
Seiichi Ibaraki [3], Kenichiro Iwakiri [3], Yoshihiro Hayashi [3]

ISROMAC 2017

International Symposium on Transport Phenomena and Dynamics of Rotating Machinery

Hawaii, Maui

December 16-21 2017

Abstract

An optimum aerodynamic design method for centrifugal compressor impeller has been developed. The present optimum design method is using a genetic algorithm (GA) and a two-dimensional inverse blade design method based on a meridional viscous flow analysis. In the meridional viscous flow analysis, an axisymmetric viscous flow is numerically analyzed on a two-dimensional meridional grid to determine the flow distribution around the impeller. Full and splitter blade effects to the flow field are successfully evaluated in the meridional viscous flow analysis by a blade force modeling. In the inverse blade design procedure, blade loading distribution is given as the design variable. In the optimization procedure, the total pressure ratio and adiabatic efficiency obtained from the meridional viscous flow analysis are employed as objective functions. Aerodynamic performance and three-dimensional flow fields in the Pareto-optimum design and conventional design cases have been investigated by three-dimensional Reynolds averaged Navier-Stokes (3D-RANS) and experimental analyses. The analyses results show performance improvements and suppressions of flow separations on the suction surfaces in the optimum design cases. Therefore, the present aerodynamic optimization using the inverse method based on the meridional viscous flow analysis is successfully achieved.

Keywords

centrifugal compressor — optimization — genetic algorithm

[1] *Department of Mechanical Engineering, Kyushu University, Fukuoka, Japan*
[2] *Mitsubishi Heavy Industries Engine & Turbocharger, Ltd., Kanagawa, Japan*
[3] *Mitsubishi Heavy Industries, Ltd., Nagasaki, Japan*
***Corresponding author**: itou@haira.mech.kyushu-u.ac.jp

INTRODUCTION

Much design methods for turbomachinery have been developed to improve aerodynamics performance such as efficiency, pressure ratio and operating range. In the recent years, inverse design and optimization methods have been receiving remarkable attention and spreading for the compressor designs.

Zangeneh has been developing the inverse design method for turbomachinery [1-3]. The design tool named Turbo Design 1 is one of the most well-known inverse blade design tools for turbomachinery. Based on the assumption of potential flow, the blade geometry is obtained by the inverse method from a predetermined blade loading distribution. Secondary flow in flow passeges of vaned diffusers, centrifugal and mixed flow impellers are successfully reduced using the Turbo design 1.

As for the optimization method, multi objective design methods for the centrifugal compressors have been developed. R.A. Van den Braembussche et al.[4] had developed an aerodynamic optimization method using an Artificial Neural Network (ANN) and a genetic algorithm (GA). The aerodynamic performance of the designed compressors was successfully evaluated by the ANN based on the three-dimensional CFD results. The optimum design method provided improvements of aerodynamic performance. In addition, the recent optimizations of the turbomachinery have been achieved by an adjoint method. Multistage design optimizations [5,6] and a multipoint design optimization were successfully performed with the adjoint method.

The authors have been developed an optimum aerodynamic design method using a meridional viscous flow analysis and applied to a diffuser augmented wind turbine design [8,9]. The rotor and diffuser geometries were simultaneously optimized and the aerodynamic performance was improved by the optimum design based on the meridional viscous flow analysis. In this paper, the optimum design method has been updated and applied to the centrifugal compressor impeller design. The remarkable feature of the present optimum design method is that the meridional viscous flow analysis performed on a two-dimensional grid is utilized to evaluate the aerodynamic performance in the procedure. Since the inverse method based on the meridional viscous flow analysis is combined with the optimization method, the optimum blade loading distributions can be obtained. Thus, global optimum blade design cases in different flow conditions may be easily obtained by the optimum blade loading distributions and the inverse method. Three-dimensional Reynolds Averaged Navier-Stokes (3D-RANS) and experimental analyses have been carried out to compare the flow fields and the aerodynamic performance between the optimum and conventional design cases.

1. AERODYNAMIC DESIGN METHOD

Figure 1 shows a flow chart of the optimum aerodynamic design optimization method. The aerodynamic design flow chart is shown on the left side of Fig. 1. The present aerodynamic design consists of the two parts: meridional viscous flow calculation and two-dimensional inverse design method. The calculation and inverse method are performed repeatedly until the blade geometry and flow field are converged. The meridional viscous flow calculation is performed on a two-dimensional meridional grid with a blade force modeling in order to obtain the flow distribution around impeller. Using the flow distribution and the predetermined blade loading distribution, the 3-D impeller geometry is obtained by the inverse method.

2. MERIDIONAL VISCOUS FLOW ANALYSIS

The meridional viscous flow calculation is introduced to determine the flow distributions around the impeller for the blade design and aerodynamic performance for the optimization. The meridional viscous flow calculation is performed based on the assumption if the axisymmetric and viscous flow. The inviscid blade effect is evaluated by a blade force modeling which is introduced as a body force to the governing equations of the meridional viscous flow calculation. The circumferential component of the blade force can be written as

$$F_{b\theta} = \rho \frac{c_m}{r} \frac{\partial r c_\theta}{\partial m} \tag{1}$$

Here c_m and c_θ represent the meridional and circumferential components of the absolute velocity, respectively, m is the distance along the meridional streamline, ρ is the density of air, r is the radius from the axis of blade rotation. All the flow quantities in the right hand side of the above equation are given as circumferentially-averaged values. The axial and radial components of the blade force, F_z and F_r, are calculated from the assumption that blade force acts perpendicular to the blade camber, because the blade force introduced in the present analysis includes no viscous force acting on the blade [8-10]. As mentioned above, the meridional viscous flow analysis is performed on the two-dimensional meridional grid. Since the geometries of the full and splitter blades are different from each other, the value of $\partial r c_\theta / \partial m$ is calculated from the averaged value of the flow angle β of the full and splitter blades. Any loss models are not included in the meridional viscous flow analysis except for the k-omega turbulence model.

The meridional viscous flow calculations in the present study are performed in the region from the compressor inlet to the diffuser outlet. The scroll region is not calculated in the present analysis. Figure 2 shows the meridional velocity and static pressure distributions in a conventional design case obtained from the meridional viscous flow analysis. The impeller geometry in the conventional design case is shown in the following sections. Boundary layers are observed on the shroud and hub surfaces in Fig. 2 (a). The actual static pressure ratio at the diffuser outlet in the conventional design case is less than 2.0. However, the static pressure ratio obtained from the meridional viscous flow analysis is higher than the actual static pressure ratio as shown in Fig. 2 (b). The excessive pressure ratio in the meridional viscous flow analysis is caused by the assumption that the slip effect and the losses such as friction loss on blade surface and tip leakage loss are not included in the meridional viscous flow analysis. The aerodynamic design and the optimization are carried out using the meridional viscous flow analysis result. The calculation time for the single meridional viscous flow analysis using Intel® CoreTM i7-3970X processor without parallelization technique is less than 10 minutes, which is significantly shorter than that for the 3D-RANS analysis.

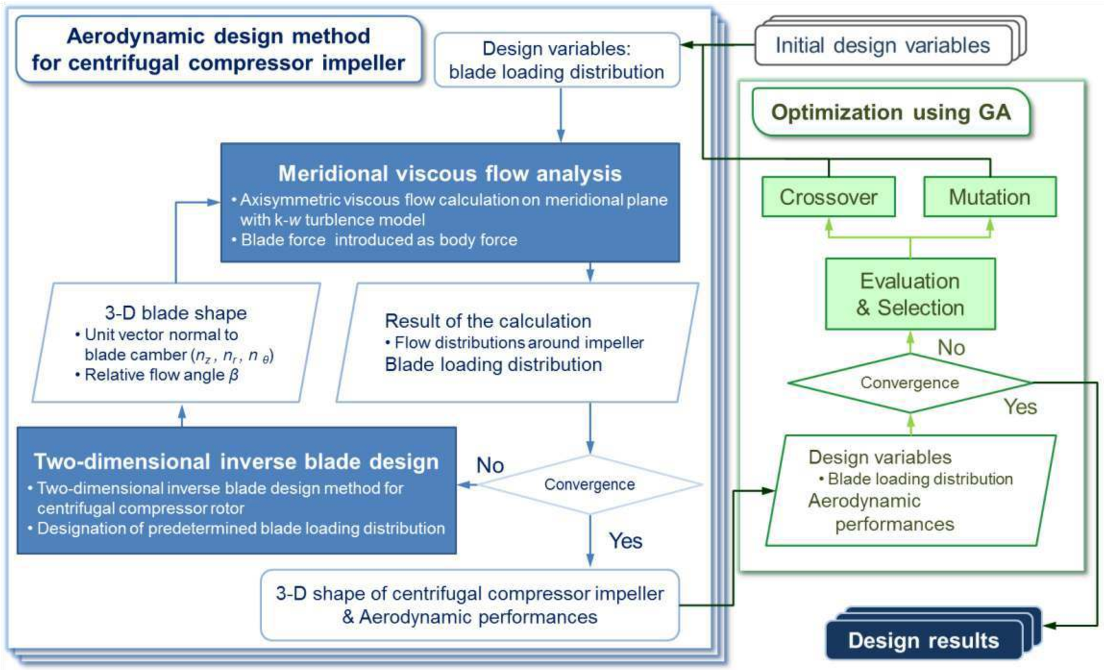

Fig. 1 Flow chart of optimum aerodynamic design method

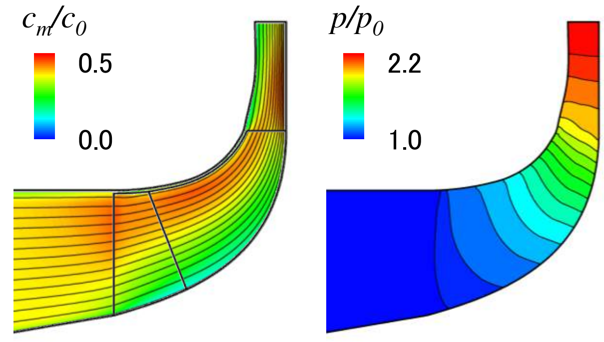

(a) Meridional velocity (b) Static pressure

Fig. 2 Meridional flow distribution in conventional design case obtained from meridional viscous flow analysis

3. TWO-DIMENSIONAL INVERSE METHOD

The 3-D impeller geometry is obtained from the meridional viscous flow calculation result and the predetermined blade loading distribution. Equations (2) and (3) give the circumferential velocity c_θ distribution inside the rotor blade. Δp_{max} is determined from the design specification.

$$c_\theta = \frac{r1}{r} c_{\theta 1} + \frac{N\Delta p_{\max}}{2\pi r}\int_{m1}^{m}\frac{F(m)}{K_b \rho c_m}\,dm \qquad (2)$$

$$\Delta p = \Delta p_{\max} F(m) \qquad (3)$$

where $F(m)$ is the normalized chordwise blade loading distribution. The circumferential velocity at the blade inlet $c_{\theta 1}$ is obtained from the meridional viscous flow calculation result. The relative flow angle β is determined from the circumferential velocity c_θ and the meridional viscous flow calculation result:

$$\beta = \tan^{-1}\left(\frac{c_\theta - r\omega}{c_m}\right) \qquad (4)$$

In this way, the camber lines are determined from the relative flow angle β distribution. The 3-D impeller geometry is constructed from the camber lines and blade thickness distributions.

4. OPTIMUM AERODYNAMIC DESIGN METHOD

The optimization flow chart by a genetic algorithm (GA) is shown on the right side of Fig. 1. In the present study, the Non-dominated Sorting Genetic Algorithm II (NAGA-II) [13] which is a well-known optimization method by its performance was used as evaluation and selection models. The Real-coded Ensemble Crossover (REX) [14] was used as a crossover model. In this optimization procedure, initial impellers are designed from randomly decided initial design specifications. The aerodynamic performance in the designed impellers is evaluated from the meridional viscous flow analysis results. Based on the design specifications are created due to the section, mutation, crossover processes. Thus, the aerodynamic optimization of impeller based on the meridional viscous flow analysis is carried out.

5. DESIGN VARIABLES

The blade loading distribution is defined by Akima interpolation method fitted to 27 points located on the meridional plane shown as red circle symbols in Fig. 3. The values of the blade loading at each 27 points are treated as the design variables. The blade loading distribution for the full and splitter blades are decided by 18 and 9 variables, respectively. The same design specifications except for the blade loading distribution, such as rotational speed, meridional geometry and number of blades are adopted in the present study.

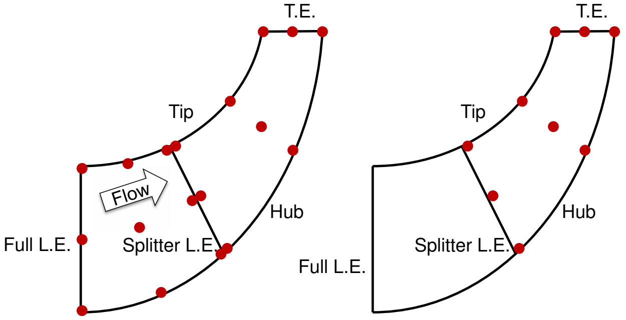

Fig. 3 Design variables locations for blade loading distributions

6. PARETO OPTIMUM DESIGN CASES

The total pressure ratio π and the adiabatic efficiency η obtained from the meridional viscous flow calculations are the objective functions for the present aerodynamic optimization.

$$\pi = p_{t3} / p_{t0} \qquad (5)$$

$$\eta = \frac{\left(p_{t3}/p_{t0}\right)^{\frac{\gamma-1}{\gamma}} - 1}{\left(T_{t3}/T_{t0}\right) - 1} \qquad (6)$$

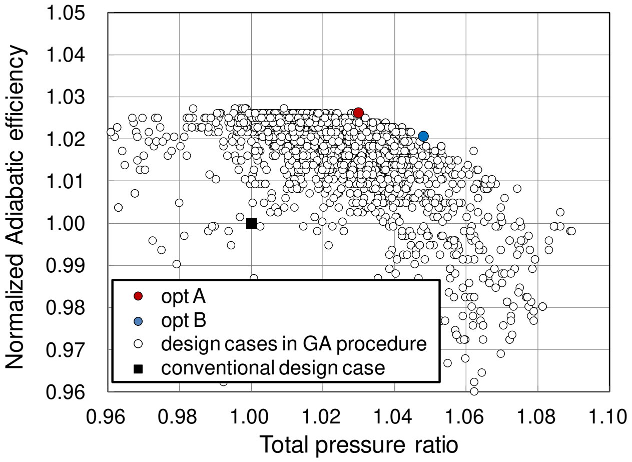

Fig. 4 Aerodynamic performance obtained from meridional viscous flow analysis results

where p_{t0} and p_{t3} are the total pressures at the inlet and the diffuser outlet, respectively. T_{t0} and T_{t3} are the total temperatures at the inlet and the diffuser outlet, respectively. Figure 4 shows the total pressure ratio π and the adiabatic efficiency η in the design and conventional cases obtained from meridional viscous flow calculations. In the figure, the ordinate denotes the adiabatic efficiency and the abscissa denotes the total pressure ratio, respectively. Pareto optimum solutions named opt A and opt B and the conventional design case are indicated as red, blue and black symbols in the figure, respectively. In this study, opt A and opt B are chosen because they locate on the Pareto front and show both high total pressure ratio and high adiabatic efficiency compared with the conventional design case. The compressor geometry for the conventional design case except for the impeller geometry is the same as that for the present optimum design cases. The figure shows the performance improvement in the optimum design cases.

Figure 5 shows the blade loading distributions for the conventional, opt A and opt B design cases. In Fig. 5, the abscissa denotes the non-dimensional chord at each span height and the ordinate denotes the blade loading *Δp* normalized by atmospheric pressure, respectively. Using the meridional viscous flow calculation result, the design blade loading distribution can be extracted from eq. (1). In addition, the blade loading distribution at the tip section in the conventional splitter blade is higher than those in the optimum design cases. On the other hand, the blade loading from the mid-chord to the trailing edge at the tip section at the conventional full blade is significantly lower. Figure 6 shows the geometry comparisons between the optimum and conventional design cases. Figure 6 indicates the inlet flow angle difference between the conventional and optimum design cases.

7. 3D-RANS ANALYSIS

As mentioned above, the present optimization is carried out using the meridional viscous flow analysis. The validation of the present optimization is performed using three-dimensional simulations and experiments. Three-dimensional flow field in the optimum and conventional design cases in one pitch region was analyzed by the 3D-RANS simulation.

The number of computational cells for the 3D-RANS analysis is about 50 million cells. The y+ condition calculated from the minimum gird spacing to the solid wall satisfied less

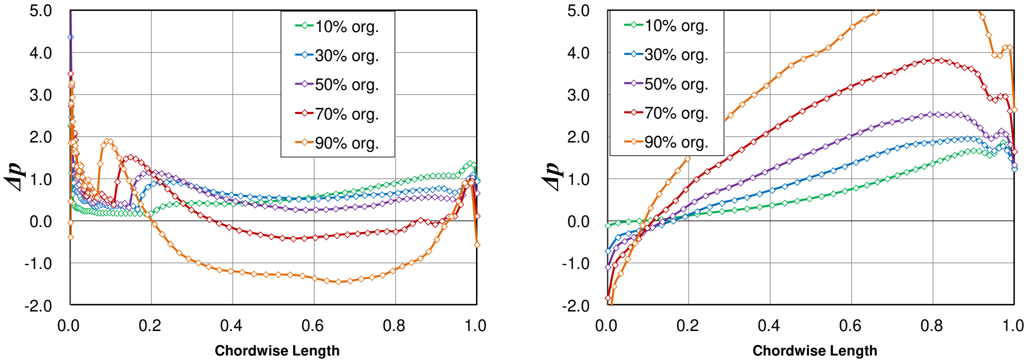

(a) conventional (full blade) (b) conventional (splitter blade)

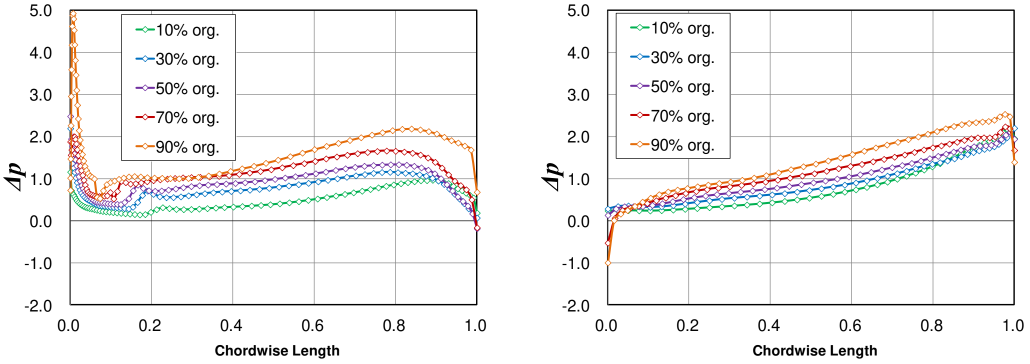

(c) opt A (full blade) (d) opt A (splitter blade)

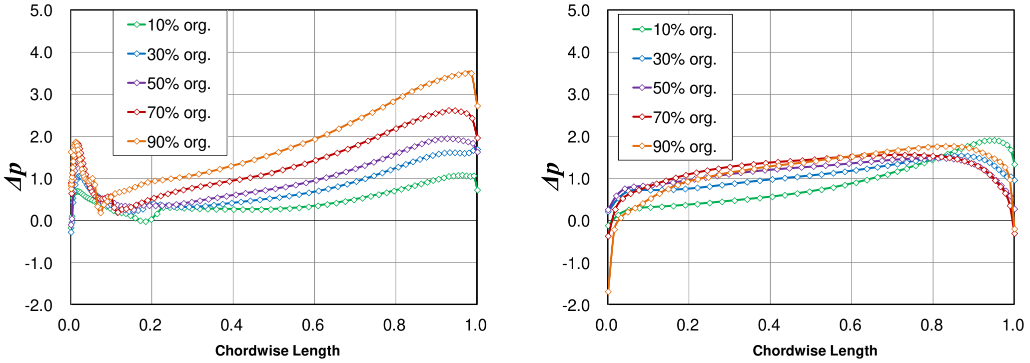

(e) opt B (full blade) (f) opt B (splitter blade)

Fig. 5 Design blade loading distributions for conventional and optimum design cases than 1. The calculation region for the 3D-RANS analysis is the same as that for the meridional calculation, namely, the scroll region is not included in the 3D-RANS and the meridional viscous flow analyses. A fully-implicit scheme with a cell-centered finite volume method based in-house CFD code was used for the 3D-RANS analysis [15,16]. The inviscid and viscid fluxes are evaluated using the SHUS (Simple High-resolution Upwind Scheme) [17] and Gauss's theorem, respectively. As for the evaluation of the eddy viscosity, the k-omega two-equation turbulence model [18] was employed.

A critical-point concept was applied to the flow visualization technique. The trajectory of the vortex core identified by the critical-point concept was colored by the normalized helicity defined as [19,20];

$$H_n = \vec{\xi}\cdot\vec{w}/\left|\vec{\xi}\right|\cdot\left|\vec{w}\right| \qquad (7)$$

where ξ and w denote vectors of the absolute vorticity and the relative flow velocity, respectively. The normalized helicity

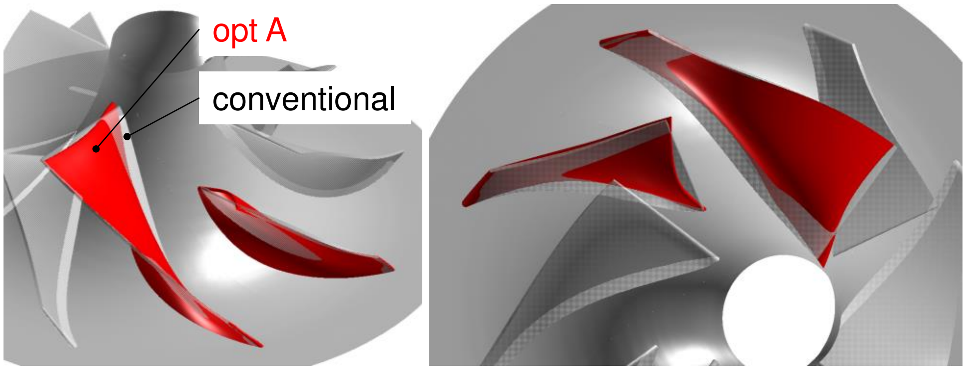

(a) Opt A and conventional design cases

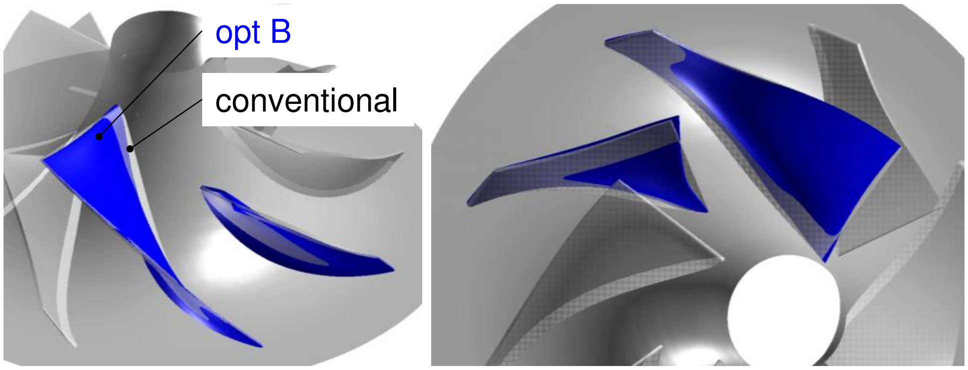

(b) Opt B and conventional design cases

Fig. 6 Impeller geometries of optimum and conventional design cases

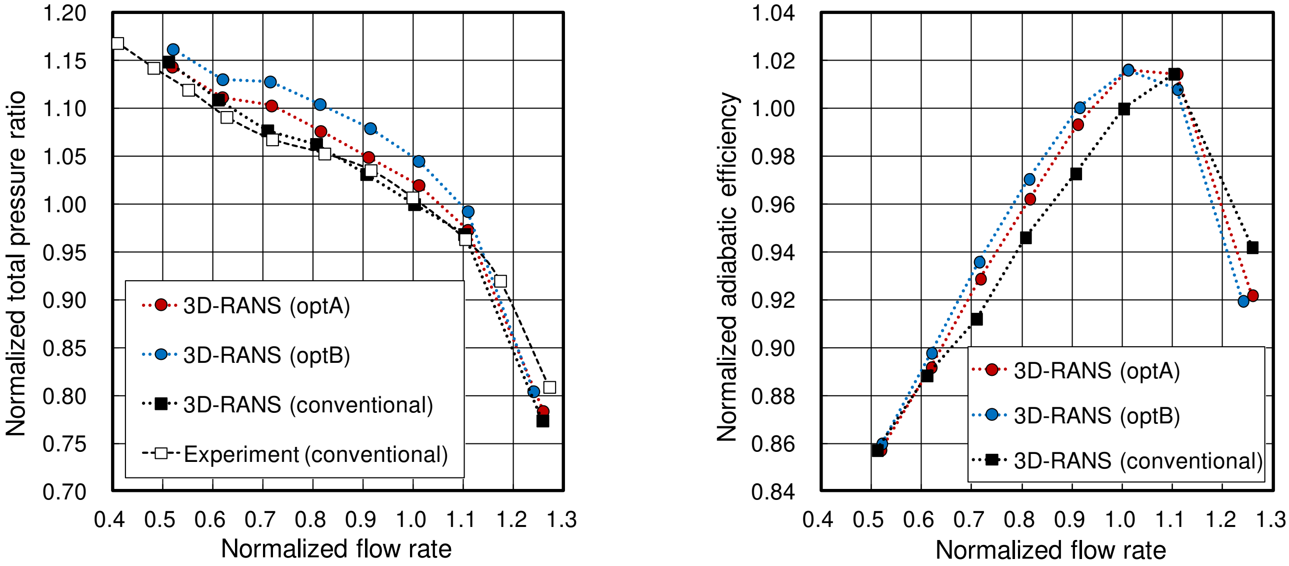

(a) Total pressure ratio (b) Adiabatic efficiency

Fig. 7 Aerodynamic performance obtained from 3D-RANS analysis results indicates the relative swirl direction of the vortex relative to the velocity component.

8. AERODYNAMIC PERFORMANCE

Figure 7 shows the aerodynamic performance in the opt A, opt B and conventional design cases obtained from 3D-RANS analysis results. In Fig. (a) and (b), the ordinates denote the normalized total pressure ratio and the normalized adiabatic efficiency, respectively. The abscissa denotes the normalized flow rate. The normalized flow rate is defined by normalizing the flow rate on the basis of the design flow rate. The total pressure ratio and the adiabatic efficiency are normalized by those evaluated from the 3D-RANS analysis of the conventional design case at the design flow rate, respectively. Figure 7 (a) includes experimental results of the total pressure ratio in the conventional design case. It can be seen from Fig. 7 (a) that the 3D-RANS analysis results of the performance characteristic in the conventional design case shows good agreement with the experimental results. The total pressure ratios in the opt A and opt B cases are superior to that in the conventional case, except the operating region around the maximum flow rate. Figure 7 (b) shows that the adiabatic efficiencies in the optimum cases are much higher than that in the conventional case, except the operating region around the maximum flow rate.

9. THREE-DIMENSIONAL VORTICAL FLOW FIELD

Figure 8 shows vortex cores identified by the critical-point concept, limiting streamlines on the blade surfaces and entropy function distributions at the impeller exit in the conventional and optimum design cases. In the figure, the vortex cores are colored by the normalized helicity defined by Eq. (7). The entropy function is defined by the following Eq. (8):

$$s^* = e^{\frac{\Delta s}{R}} = \frac{\left(T_t / T_{t0}\right)^{\frac{\gamma}{\gamma-1}}}{p_t / p_{t0}} \tag{8}$$

As seen in Fig. 8, tip leakage vortices are observed from the leading edges of the full and splitter blades in each design case. In addition, leading edge separations on the blade suction surfaces are also observed. The tip leakage vortices and the leading edge separation vortices cause loss generations as seen in the entropy function distributions at the impeller exit. Figures 8 (b) and (c) indicate that the loss

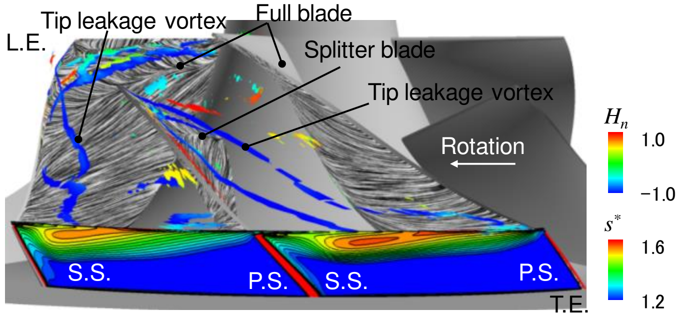

(a) conventional

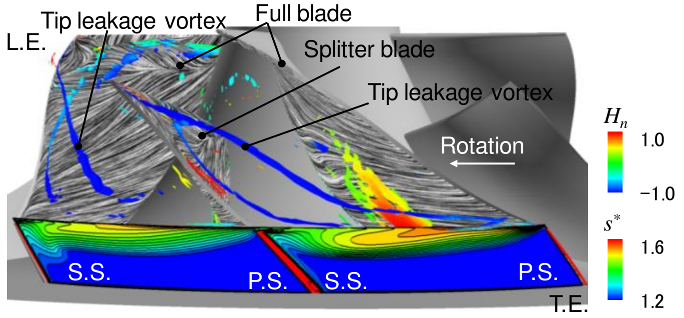

(b) opt A

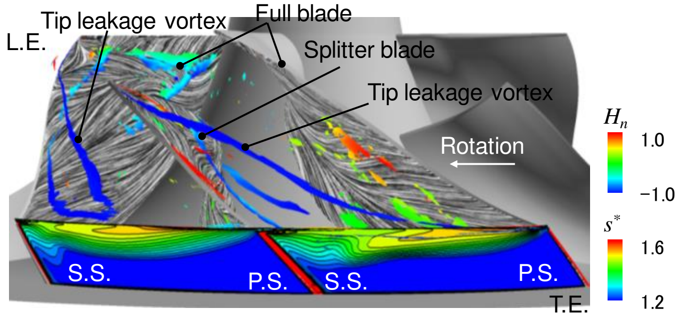

(c) opt B

Fig. 8 Vortex structures around impeller, limiting stream lines on impeller surface and entropy function distribution at impeller exit

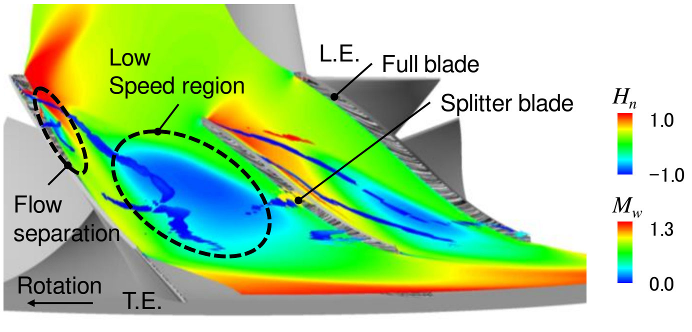

(a) conventional

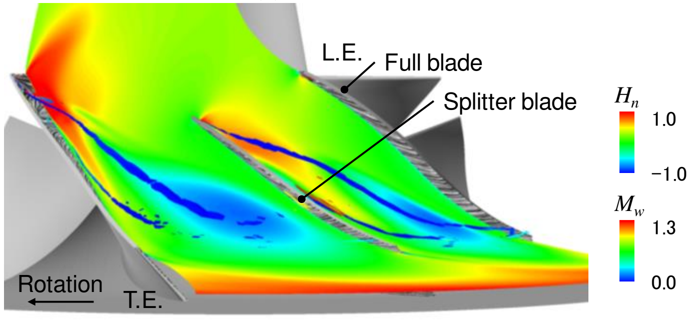

(b) opt A

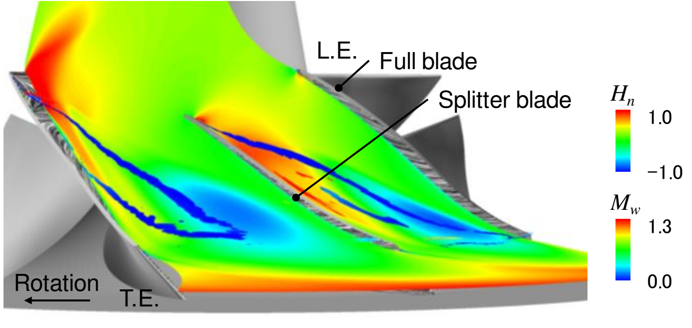

(c) opt B

Fig. 9 Relative Mach number distribution at 90 percent span height and vortex structures around impeller generations are successfully suppressed in the optimum design cases, compared with the conventional design case shown in Fig. 8 (a).

Figure 9 shows relative Mach number distributions at 90 percent span height and vortex structures in the conventional and optimum design cases. As shown in Fig. 9, shock waves near the leading edge of the full blades and low Mach number regions near the mid chord of the full blades are observed. Especially in the conventional case, the low Mach number region is widely distributed. In addition, the flow separation is observed in the boundary layer on the conventional full blade suction surface near the leading edge. In the optimum design cases, on the other hand, the boundary layer thicknesses on the full blade suction surface are thinner than that in the conventional design case. In other words, the low velocity area expansion in the conventional design case is caused by the leading edge separation on the full blade suction surface. In the optimum design cases, the blade loading at the full blade inlet is relatively smaller than that in the conventional case as shown in Fig. 5. As a result, in the optimum design cases the large scale leading edge separation is suppressed so that the low Mach number region becomes smaller.

Figure 10 shows the comparison of pitch-wise averaged flow distributions at the full blade inlet for the 80 percent design flow rate. In Fig. 10 (a), the abscissa denotes the axial mass flux normalized by the density and the speed of sound at the upstream stagnation state, and the ordinate denotes the span height normalized by the inlet passage height. As shown in Fig. 10 (a), the flows in the optimum design cases are accelerated on the blade tip side compared with the flow in the conventional design case. The flow in the opt B case is, however, different from the one in the opt A case. The flow from the tip to the mid-span in the opt B case is uniform. On the other hand, in the opt A design case, that is not uniform and the flow near 80 percent span height is most accelerated.

In Fig. 10 (b), the abscissa denotes the incidence angle at the full blade and the ordinate denotes the span height normalized by the inlet passage height. In the opt A design case, comparing with the conventional design case, the incidence angle is reduced at the tip and on the hub side but it is increased at the mid-span. In the opt B design case, the incidence over the whole span height is comparatively lower than one in the conventional design case.

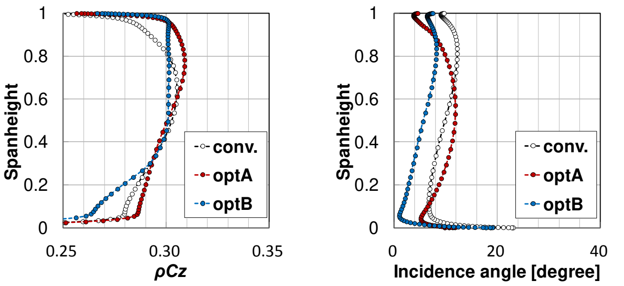

(a) Axial mass flux (b) Incidence angle

Fig. 10 Pitch-wise averaged flow distributions at full blade inlet (80 percent design flow rate)

Figure 11 shows the vortex cores identified by the critical-point concept, the limiting streamlines on the blade suction surfaces and the entropy function distributions on the full blade suction surface at the 80 percent design flow rate in the conventional and optimum design cases. In the figure, the vortex cores are colored by the normalized helicity defined by Eq. (7). The entropy function is defined by Eq. (8). In Fig. 11, the differences in the leading edge separation vortex and the limiting streamlines between the conventional and optimum design cases are observed. As shown in Fig. 11 (a), the radially outward flow is observed in the limiting streamlines near the leading edge. In optimum design cases, the radially outward flow is suppressed near the leading edge. Especially near the hub side of the leading edge in the opt B, where the incidence angle is approximately zero as shown in Fig. 10 (b), and the leading edge separation and the radially

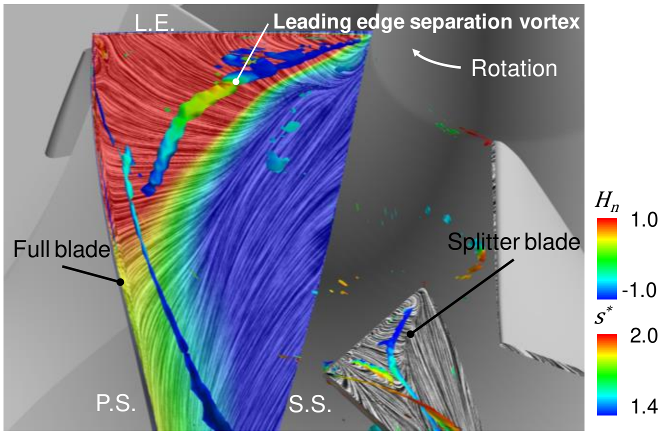

(a) conventional

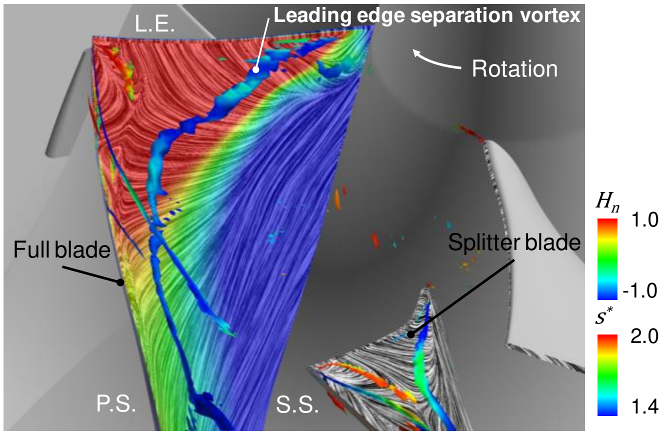

(b) opt A

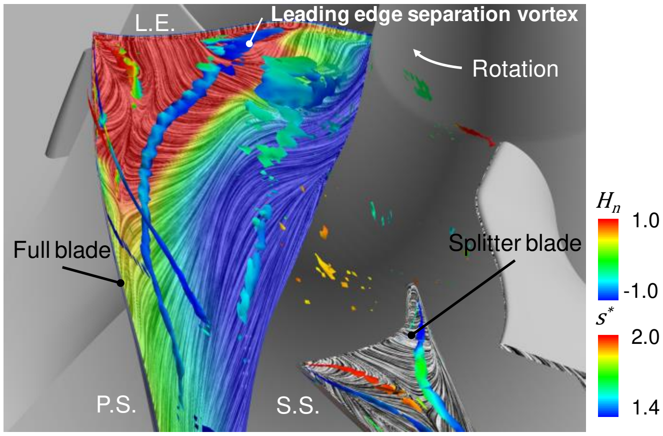

(c) opt B

Fig. 11 Vortex structures around impeller, limiting stream lines on impeller surface and entropy function distribution at impeller inlet (80 percent design flow rate) outward flow are not observed because of the decrease in the incidence angle of the opt B. These facts results in the decrease in the leading edge separation region corresponding to the high entropy function region shown in Fig. 11 (c) and the suppression of the high-loss fluid accumulation at the impeller outlet shown in Fig. 8 (c) in the opt B design case. As a result , the adiabatic efficiency of the opt B case at 80 percent design flow rate is higher than the other design cases as shown in Fig. 7 (b).

10. EXPERIMENTAL ANALYSIS

One of the Pareto optimum design cases called opt B, which has the highest aerodynamic performance at the reference operating point obtained from the 3D-RANS analysis results, has been investigated by experimental analysis. The experimental analyses were carried out at the test facility in the R/D center, Mitsubishi Heavy Industries, Ltd.. The compressor cover which defines shroud and scroll geometries for the optimum design case is the same as that for the conventional one. Figure 12 shows the aerodynamic performance in the opt B and the conventional design cases obtained from experimental analysis results. The abscissa in Fig. 10 denotes the relative flow rate, the ordinate in Fig. 12 (a) denotes the relative total pressure ratio and the ordinate in Fig. 12 (b) denotes the relative adiabatic efficiency, respectively. The values of the pressure ratio, the adiabatic efficiency and the flow rate in Fig. 12 are normalized by those at the operating point which has the highest adiabatic efficiency in the conventional design case, respectively. As shown in Fig. 12, the values of the total pressure ratio in the opt B case are superior to those in the conventional case. However, surging flow rate in the opt B case is higher than that in the conventional case. As shown in Fig. 12, the values of the adiabatic efficiency around the reference flow rate in the opt B case are slightly higher than those in the conventional case. In the meridional viscous flow analysis and the 3D-RANS analysis, the aerodynamic performance is evaluated from the pressure and the temperature at the inlet region and the diffuser outlet. On the other hand, the measurement point for the outlet pressure and temperature in the experiments is located at the scroll exit. There may be a possibility that the scroll performance deteriorated, because of the excessive pressure rise in the opt B case.

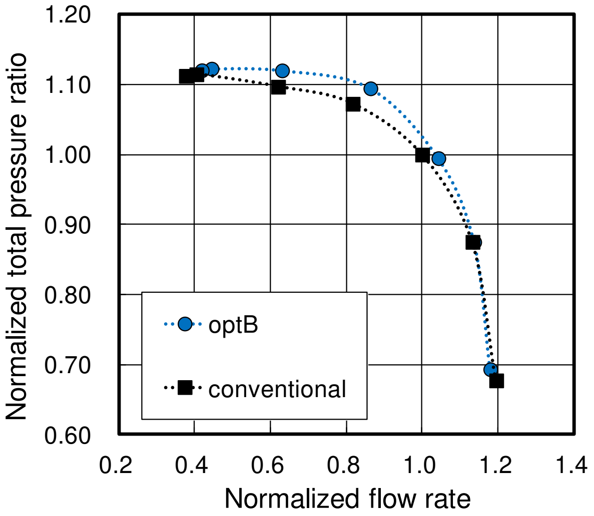

(a) Total pressure ratio

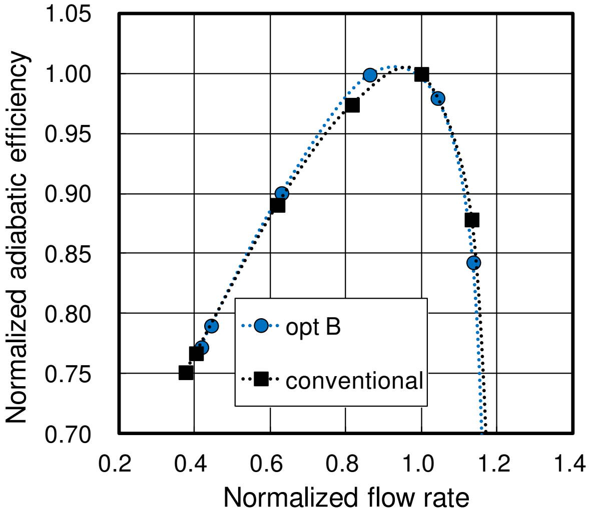

(b) Adiabatic efficiency

Fig. 12 Aerodynamic performance obtained from experimental analysis results

11. CONCLUSION

The optimum aerodynamic design method using the genetic algorithm (GA) and the two-dimensional inverse method based on the meridional viscous flow analysis has been applied to the centrifugal compressor impeller. The three-dimensional Reynolds-averaged Navier-Stokes (3D-RANS) analysis and experimental analysis has been performed to investigate the validity of the present design method. The results are summarized as follows:

(a) The two-dimensional inverse blade design method consists of the meridional viscous flow analysis and the two-dimensional inverse analysis. In the meridional viscous flow analysis, the axisymmetric Reynolds-averaged Navier-Stokes equations with the blade force model are numerically solved on the two-dimensional meridional grid to determine the flow distribution around the impeller and evaluate the aerodynamic performance. In the two-dimensional inverse analysis, the impeller geometry is designed from the blade loading distribution and the meridional viscous flow analysis result.

(b) Using the present optimization method, the optimum impeller geometries and the blade loading distributions were obtained. The blade loading from the mid-chord to the trailing edge at the tip section at the conventional full blade is significantly lower than that of optimum design cases.

(c) The total pressure ratios and the adiabatic efficiencies in the Pareto-optimum design cases obtained from the results of the 3D-RANS analyses and the experiments are higher than those in the conventional design case. The results of the 3D-RANS analyses indicate that the aerodynamic performance improvements in the Pareto-optimum design cases are achieved by the optimum blade loading distributions. The reduction of the blade loading at the leading edges and the tip sections suppress the loss generation from the leading edge separation and the tip leakage vortex.

NOMENCLATURE

c :	absolute velocity
F_b :	blade force
$F(m)$:	normalized blade loading distribution for design
H_n :	normalized helicity
K_b :	blockage factor
m :	meridional length
N :	number of blade
p :	pressure
p_t :	total pressure
r :	radius
R:	gas constant
s:	entropy
s^*:	entropy function
T_t :	total temperature
u :	rotor speed
w :	relative velocity
γ:	ratio of specific heat
η :	adiabatic efficiency
ξ :	relative vorticity
π :	pressure ratio
ρ :	density of air

SUBSCRIPTS

0 :	inlet
1 :	impeller leading edge
2 :	impeller trailing edge
3 :	diffuser outlet
m :	meridional component
r :	radial component
z :	axial component
θ :	circumferential component

ACKNOWLEDGMENTS

The present research was partially supported by the Turbomachinery Society of Japan.

REFERENCES

[1] Zangeneh, M., 1991, “A Compressible Three Dimensional Blade Design Method for Radial and Mixed Flow Turbomachinery Blades,” Int. J. Numerical Methods in Fluids. Vol. 13, pp. 599-624.

[2] Zangeneh, M., Ejiri, E., and Kubo, M., 1997, “On 3 D Inverse Design of an Automotive Torque Converter Pump Impeller in Shear Flow,” Proceedings of JSME International Conference on Fluid Engineering, pp. 201-206.

[3] Zangeneh, M., Goto, A. and Harada, H., 1998, “On the Design Criteria for Suppression of Secondary Flows in Centrifugal and Mixed Flow Impellers,” ASME Journal of Turbomachinery, Vol. 120, pp. 723-735.

[4] Van den Braembussche, R., A., Alsalihi, Z., Matsuo, A., Ibaraki, S., Sugimoto, K., Tomita, I., 2012, ”Multidisciplinary Multipoint Optimization of a Transonic Turbocharger Compressor,” Proceedings of ASME Turbo Expo 2012, Paper No. GT2012-69645.

[5] Wang, D., and He, L., 2010, “Adjoint Aerodynamic Design Optimization for Blades in Multi-Stage Turbomachines: Part 2—Validation and Application,” ASME Journal of Turbomachinery, Vol. 132, No. 2, Paper No. 021012. doi:10.1115/1.3103928

[6] Walther, B., and Nadarajah, S., 2013, “Constrained Adjoint-Based Aerodynamic Shape Optimization of a Single-Stage Transonic Compressor,” ASME Journal of Turbomachinery, Vol. 135, No. 3, Paper No. 021017. doi:10.1115/1.4007502

[7] Luo, J., Zhou, C., and Liu, F., 2014, “Multi-Point Design Optimization of a Transonic Compressor Blade by Using an Adjoint Method,” ASMEJournal of Turbomachinery, Vol. 136, No. 5, Paper No. 051005. doi:10.1115/1.4025164

[8] Oka, N., Furukawa, M., Yamada, K., and Kido, K., 2013, “Aerodynamic Design for Wind-Lens Turbine Using Optimization Technique,” Proceedings of the ASME 2013 Fluids Engineering Summer Meeting, Paper No. FEDSM2013-16569.

[9] Oka, N., Furukawa, M., Kawamitsu K., and Yamada, K., 2016, “Optimum aerodynamic design for wind-lens turbine,” Journal of Fluid Science and Technology 11(2):JFST0011, DOI: 10.1299/jfst.2016jfst0011

[10] Tabata, S., Hiratani, F., and Furukawa, M., 2007, “Axisymmetric Viscous Flow Modeling for Meridional Flow Calculation in Aerodynamic Design,” Memories of the Faculty of Engineering, Kyushu Univ. Vol.67, No.4, pp. 199-208.

[11] Yamada, K., Furukawa, M., Shibata, T., Nakakido, S., Oka, N, 2014, “Supression of Secondary Flows in an Axial Flow Turbine Rotor with a Novel Design Concept,” ASME Paper, GT2014-25630.

[12] Oka, N., Furukawa, M., Yamada, K., Tamura, Y., Yamada S., Tadokoro, T., Homma, N., 2015, “Improvement in Aerodynamic Performance of a Half-Ducted Axial Flow Fan using Meridion Viscous Flow Analysis,” The 13th Asian International Conference on Fluid Machinery, AICFM13-073

[13] Kalyanmoy, D., Associate Member, IEEE, Amrit, P., Sameer, A., and T. Meyarivan, 2002, “A Fast and Elitist Multiobjective Genetic Algorithm:NSGA-II,” IEEE Trans. on evolutional computation, Vol. 6, No. 2, pp.182-197.

[14] Kobayashi, S., 2009, “The frontiers of real-coded genetic algorithms,” Journal of the Japanese Society for Artificial Intelligence, Vol24, No.1, pp.147-162.

[15] Yamada, K., Furukawa, M., Fukushima, H., Ibaraki, S., Tomita, I., 2011, “The Role of Tip Leakage Vortex Breakdown in Flow Fields and Aerodynamic Characteristics of Transonic Centrifugal Compressor Impellers,” ASME Paper, GT2011-46253.

[16] Yamada, K., Furukawa, M., Nakano, T., Inoue, M., and Funazaki, K., 2004, “Unsteady three-dimensional flow phenomena due to breakdown of tip leakage vortex in a transonic axial compressor rotor,” ASME Paper GT2004-53745.

[17] Shima, E., and Jounouchi, T., 1997, “Role of CFD in Aeronautical Engineering (No.14) -AUSM Type Upwind Schemes,” the 14th NAL Symposium on Aircraft Computational Aerodynamics, NAL SP-34, pp. 7-12

[18] Wilcox, D. C., 1988, “Reassessment of the Scale-Determining Equation for Advanced Turbulence Models,” AIAA Journal, Vol.26, No.11, pp.1299-1310.

[19] Sawada, K., 1995, “A Visualization Method for Identifying Vortex Centers,” Trans. Japan Soc. of Aero Space Sci., Vol.38, No.120, pp.102-116.

[20] Furukawa, M., Inoue, M., Saiki, K., and Yamada, K., 1999, “The Role of Tip Leakage Vortex Breakdown in Compressor Rotor Aerodynamics,” Trans. of the ASME, Journal of Turbomachinery, Vol. 121, No. 3, pp. 469–480.